

Sparse Tensor-based Multiscale Representation for Point Cloud Geometry Compression

Jianqiang Wang, Dandan Ding, Zhu Li, Xiaoxing Feng, Chunlong Cao, and Zhan Ma

Abstract—This study develops a unified Point Cloud Geometry (PCG) compression method through Sparse Tensor Processing (STP) based multiscale representation of voxelized PCG, dubbed as the SparsePCGC. Applying the STP reduces the complexity significantly because it only performs the convolutions centered at Most-Probable Positively-Occupied Voxels (MP-POV). And the multiscale representation facilitates us to compress scale-wise MP-POVs progressively. The overall compression efficiency highly depends on the approximation accuracy of occupancy probability of each MP-POV, e.g., $p_{\text{MP-POV}}$. Thus, we design the Sparse Convolution based Neural Networks (SparseCNN) consisting of sparse convolutions and voxel re-sampling to extensively exploit priors. We then develop the SparseCNN based Occupancy Probability Approximation (SOPA) model to estimate the $p_{\text{MP-POVs}}$ in a single-stage manner only using the cross-scale prior or in multi-stage by step-wisely utilizing autoregressive neighbors. Besides, we also suggest the SparseCNN based Local Neighborhood Embedding (SLNE) to characterize the local spatial variations as the feature attribute to improve the SOPA. Our unified approach shows the state-of-art performance in both lossless and lossy compression modes across a variety of datasets including the dense PCGs (8IVFB, OwlII) and the sparse LiDAR PCGs (KITTI, Ford) when compared with the MPEG G-PCC and other popular learning-based compression schemes. Furthermore, the proposed method presents lightweight complexity due to point-wise computation, and tiny storage desire because of model sharing across all scales. We make all materials publicly accessible at <https://github.com/NJUVISION/SparsePCGC> for reproducible research.

Index Terms—Point cloud geometry compression, Sparse Tensor, Sparse convolution, Multiscale Representation, Occupancy Probability Approximation, Neighborhood Embedding

1 INTRODUCTION

Having its outstanding flexibility for representing 3D objects realistically and naturally, Point Cloud (PC) has become a popular media format used in vast applications, such as the Augmented/Virtual Reality (AR/VR), autonomous driving, cultural e-heritage, and digital twin, for immersive service enabling. It then urgently calls for high-efficiency compression of point cloud, both lossy and losslessly [1]. This work first exemplifies the development of *lossless compression* in details since existing industrial applications demand such functionality for efficiently archiving point cloud-based digital assets, such as the 3D building information models used in digital twin [2], and for enforcing safety-critical system using high-precision 3D point cloud maps in autonomous machine. Later then, we show that the same architecture can be extended for *lossy compression* as well.

A point cloud is a collection of non-uniformly and sparsely distributed points that are characterized using their 3D coordinates (e.g., (x, y, z)) and attributes (e.g., RGB colors, reflectances) if applicable. Unlike those well-structured pixel grids of a 2D image plane or video frame, point cloud relies on unconstrained displacement of points to freely represent arbitrary-shaped 3D objects. However, this

puts obstacles on efficient coding of geometric occupancy due to the difficulty in characterizing and exploiting inter-correlation across spatially scattered points in a 3D space. Thus the main focus of this paper is Point Cloud Geometry (PCG) compression. For the sake of simplicity we start our discussion from the lossless mode of dense Point Cloud Geometry Compression (PCGC), and then extend the studies to other scenarios.

1.1 Background

Usually, the compression efficiency of visual data, e.g., a pixel in a 2D image or a point in a point cloud, is closely related to its entropy probability approximation conditioned on autoregressive spatial neighbors [3], having the compressed entropy $R_{\vec{v}_k}$ briefed as

$$R_{\vec{v}_k} = \mathbb{E}[-\log_2 p_{\vec{v}}(\vec{v}_k | \vec{v}_{k-1}, \vec{v}_{k-2} \dots \vec{v}_{k_0})]. \quad (1)$$

Here, \vec{v}_k is the k -th element for compression, and $\vec{v}_{k-1}, \vec{v}_{k-2}, \dots, \vec{v}_{k_0}$ are causal neighbors. $p_{\vec{v}}(\vec{v}_k | \vec{v}_{k-1}, \vec{v}_{k-2} \dots \vec{v}_{k_0})$ is the conditional probability of \vec{v}_k which directly determines the $R_{\vec{v}_k}$ (and thus the coding efficiency). A well-known example is the Context Adaptive Binary Arithmetic Coding (CABAC) [3] used in modern coding standards, where the conditional probability is derived by carefully engineered *context models*. The more precise the context modeling is, the closer probability distribution to the real data is, and the less bits consumption is.

In compression of 2D images or video frames, because their spatially-connected pixels are mostly well-arranged following local structural patterns on a 2D plane, we can

J. Wang and Z. Ma are both with the School of Electronic Science and Engineering, Nanjing University, Nanjing, Jiangsu 210093, China. Emails: wangjq@mail.nju.edu.cn, mazhan@nju.edu.cn.

D. Ding is with Hangzhou Normal University, Hangzhou, Zhejiang, China. Email: dandanding@hznu.edu.cn

Z. Li is with the University of Missouri, Kansas City, MO 64110, USA. Email: zhu.li@ieee.org.

X. Feng and C. Cao are with the Jiangsu Longyuan Zhenhua Marine Engineering Co., LTD., Nantong, Jiangsu, China. Emails: fengxiaoxing@zpmc.com, 25519785@qq.com

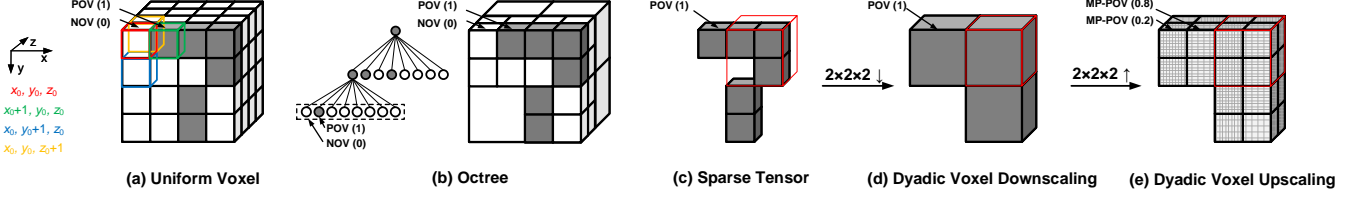


Fig. 1: **Various Representation Models of Voxelized PCG:** (a) uniform voxel; (b) occupancy driven octree decomposition; (c) sparse tensor; (d) dyadic voxel downscaling $S : 2 \times 2 \times 2 \downarrow$ from (c); (e) dyadic voxel upscaling $S : 2 \times 2 \times 2 \uparrow$ from (d) to generate MP-POVs (dense grid pattern) and associated occupancy probability, e.g., $MP-POV(p_{MP-POV})$. Voxel grids with solid line are all involved in computation. *Solid grey voxels are positively occupied, a.k.a., POVs; and the rest are NOVs, in (a) and (b). Red box in (c), (d), (e) contains spatially-connected voxels in resampling. Voxels painted with dense grid pattern are MP-POVs.*

model the “context” by conveniently accessing neighborhood pixels [4] to exploit inter-correlation. However, for an input PCG, its non-uniformly distributed 3D points do not hold explicit connections between each other, making it difficult to examine the spatial dependency in the 3D neighborhood. Therefore, we need to specify 3D representation models first to characterize the inter-point relations for 3D spatial neighborhood generation.

3D Representation Model of PCG. The very first way is to voxelizing the original point cloud into a volumetric presentation with a densely-sampled uniform voxel grid (see Fig. 1a). We call it “uniform voxel” representation for convenience. We then use *binary occupancy status* (or occupancy status) to describe whether the geometric position of the current voxel is positively occupied or not. For those Positively-Occupied Voxels (POVs) painted in solid grey in Fig. 1, they are often marked using indicators like “1” or “TRUE”; Oppositely, those Non-Occupied (empty) Voxels (NOVs) in white box in Fig. 1, are often indicated using “0” or “FALSE” flag. Note that those POVs are converted from raw “points” of an original PCG by voxelization.

As seen, this uniform 3D voxel model for PCG can be deemed as the extension of densely-sampled 2D pixel grids for the image plane. It sets up explicit neighborhood connections and allows us to access 3D spatial neighbors easily. For a NOV at (x_0, y_0, z_0) highlighted in red box (see Fig. 1a), its neighbors include a POV at $(x_0 + 1, y_0, z_0)$ contained in green box and a NOV at $(x_0, y_0, z_0 + 1)$ in yellow box.

In practice, the distribution of POVs is often very sparse. Hence, the uniform voxel representation is redundant apparently. A more efficient octree model [5] is then utilized to recursively decompose the volumetric PCG, as shown in Fig. 1b. This octree-decomposed PCG can be organized using a tree structure, where only those nodes having POVs will be sub-divided into eight sub-nodes, and so forth till the arrival of the leaf.

Adaptive Context Modeling Using Spatial Neighbors. Either uniform voxel or octree representation lets us leverage available spatial neighbors to construct a more precise context for entropy modeling. For example, in recently-approved ISO/IEC MPEG (Moving Picture Experts Group) Geometry-based PCC (G-PCC) standard [1], [6], the conditional probability of current POV is approximated using neighbors specified by parent-child connections in an octree presentation through a set of heuristic rules.

Recently, built upon the powerful expressive capacity of Deep Neural Networks (DNNs) in characterizing correlations across local spatial neighbors, a variety of learnt solutions have been developed to approximate the conditional probability of a given POV for better compression. For instance, stacked dense 3D DNNs are directly applied to uniform voxel formatted PCG to capture the dependency across voxels within current receptive field [7]–[10], by which we can set up the context modeling using masked 3D Convolutional Neural Networks (CNN) [11]. Similarly, the DNNs can be also used to improve the context modeling of octree nodes as discussed in [12]–[14].

Though these 3D DNN models improve the compression efficiency [7]–[10], [12]–[14], their huge complexity consumption hinders the prompt technology adoption and enabling. On the other hand, alternative point-wise processing methods¹ [15]–[17] using PointNet++ [18] or Multi-Layer Perceptron (MLP) report lightweight complexity consumption, but their compression performances suffer [17]. More importantly, these learnt approaches cannot easily generalize themselves to various scenarios, such as the support of both dense and sparse point clouds, and both lossy and lossless modes.

Future Prospects. After the conclusion of the G-PCC [6], international standardization groups, such as the ISO/IEC MPEG, and ISO/IEC JPEG (Joint Photographic Experts Group) are actively pursuing the next-generation point cloud compression using learning-based approaches [19], [20], which urges a solution with *better coding efficiency, affordable complexity, and robust model generalization* at the same time. Towards this goal, a more efficient 3D representation method and a better spatial neighbor utilization mechanism for adaptive context modeling are highly desired.

1.2 Our Approach

Following the conventions used in standardized G-PCC [1] and other prevalent learning-based PCGC methods [7]–[9], this study uses voxelized PCG for processing.

1. Note that aforementioned uniform voxel representation, and octree decomposition do require the voxelization to pre-process raw input, while currently these point-wise methods do not necessarily need this step.

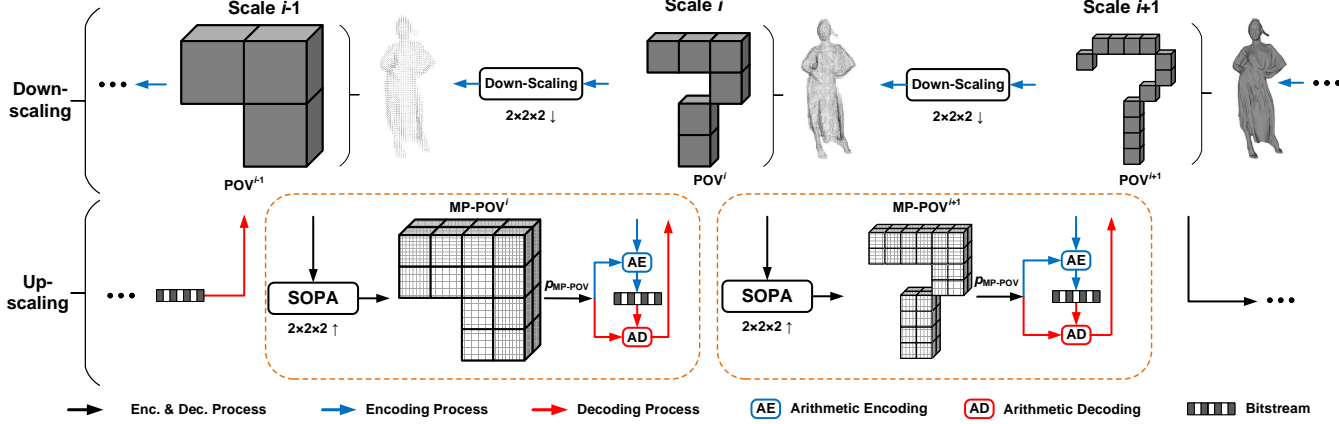


Fig. 2: **SparsePCGC**. In encoding process (blue arrows), we progressively downscale the PCG tensor and encode occupied voxels at each scale according to their occupancy probability into the binary stream; As for the decoding flow (red arrows), we extractly reconstruct occupied voxels, e.g., POV or NOV, by decoding the binary bits with the occupancy probability. The key component, a.k.a., occupancy probability approximation, that plays a vital role for coding efficacy is developed by utilizing the cross-scale and autoregresssive priors and is plugged in both encoder and decoder for bit-wise match. Such SparseCNN based Occupancy Probability Approximation is referred to as the “SOPA”. The SOPA can be fulfilled through either single-stage or multi-stage means, which fully depends on the performance and complexity trade-off.

1.2.1 Sparse Tensor Processing-Based Multiscale Representation Model

Facing those non-uniformly distributed POVs of an input PCG, this paper proposes the *Sparse Tensor Processing* (STP) framework to best utilize the sparsity of POVs.

Sparse Tensor & SparseCNN. We suggest the *Sparse Tensor Representation* for voxelized PCG, by which we only cache the geometric coordinates and attributes (if applicable) for Most-Probable POVs, i.e., MP-POVs. These MP-POVs are generated from POVs of preceding lower scale through voxel upscaling, as shown in Fig. 1e.

On the contrary, as 3D uniform voxel representation has to store all voxels, e.g., all POVs and NOVs in Fig. 1a, regardless of the occupancy status, it apparently incurs a large amount of redundancy in both space and time dimension by involving NOVs in computations.

Though octree model utilizes the voxel occupancy to adaptively decompose the input PCG, its efficiency is limited for densely-sampled sequences because it needs a deep tree hierarchy to represent fine-grained details and cannot fully leverage the advantage of octree format.

Upon the sparse tensor, we further stack *sparse convolutions* to form SparseCNN to layer-wisely process MP-POVs for accurately characterizing neighborhood correlation in a 3D space. As such, we hope to best model the spatial variations, e.g., the inter-voxel correlation, for better conditional context modeling in compression.

Enforcing the computation upon limited MP-POVs leads to a tremendous reduction of both computational complexity and storage in comparison to regular 3D dense convolutions. On the other hand, recent explorations [21] have shown that SparseCNN presents very promising performance for point cloud-based tasks, such as semantic segmentation and object detection, but there still lacks systematic studies for point cloud coding using SparseCNN.

Multiscale Representation. We use the SparseCNN

based framework to fulfill the PCGC task. In this setup, we progressively downscale the original PCG into multi-resolution PCGs, and upscale correspondingly for scalable reconstruction, as illustrated in Fig. 2.

We simply apply the *dyadic voxel sampling* to upscale or downscale related sparse tensor, which basically performs the upscaling or downscaling with a stride of 2 at each axis (e.g., x -, y - and z -axis). For convenience, we regard the $S : 2 \times 2 \times 2 \uparrow$ as dyadic voxel upscaling, and $S : 2 \times 2 \times 2 \downarrow$ as dyadic voxel downscaling.

- As for the downscaling in encoding, we merge eight spatially-connected sub-voxels contained in a $2 \times 2 \times 2$ box to a single voxel (see Fig. 1d). If any one out of these eight sub-voxels is a POV, the merged voxel is a POV. In encoder, we have full knowledge of each POV (i.e., occupancy status) at each scale.
- As for the upscaling in decoding, we sub-divide a specific voxel to eight sub-voxels (see Fig. 1e). If this voxel is a POV², its sub-voxels after sub-division are marked as MP-POVs since we cannot guarantee which sub-voxel is positively occupied just right after the upscaling process. Ideally, the collection of MP-POVs is a superset of POVs.

Such voxel sampling is often integrated with SparseCNN to aggregate and embed neighborhood information in the feature domain for better performance, in comparison to the direct scaling in the voxel domain. As seen, voxel sampling enables the resolution scalability, as is so-called *multiscale representation*.

1.2.2 Cross-Scale Context Modeling

The proposed SparsePCGC encodes the occupancy of MP-POVs at each scale into a compressed bitstream and corre-

2. We actually know the ground-truth after decoding in lossless compression because the sparse tensor in encoder and decoded tensor in decoder have to be the same.

spondingly it decodes the binary bits for the reconstruction of POVs at the same scale. For either lossy or lossless compression, the occupancy probability approximation of each MP-POV is critical to the performance of SparsePCGC.

Built upon the multiscale representation model, we propose to perform the cross-scale context modeling by utilizing decoded POVs (e.g., occupancy status and feature attribute if applicable) from preceding lower scale to approximate the occupancy probability of each MP-POV at the current scale.

Note that the cross-scale context modeling is limited between two consecutive scales only. This allows us to train models just using samples from two consecutive scales and then apply them for inference across all scales. Such cross-scale model sharing would reduce the complexity significantly.

One-Stage SOPA. Dyadically upscaling a decoded POV will generate eight spatially-connected MP-POVs (see Fig. 1e). As a toy baseline, we apply a single-stage SOPA to approximate the occupancy probabilities of eight upscaled MP-POVs in one-shot.

Multi-Stage SOPA. Previous one-shot occupancy probability derivation does not fully exploit inter-correlation among these spatially-connected MP-POVs. Thus, we suggest the multi-stage SOPA to step-wisely approximate the occupancy probabilities of grouped MP-POVs from one group to another. Here, we carefully examine three typical scenarios: *n*-Stage, 8-Stage, and 3-Stage.

For *n*-Stage, it processes all upscaled MP-POVs one-by-one in a 3D raster scanning order by making the probability estimation conditioned on autoregressive neighbors, which offers the highest coding performance but the decoding time is unbearable due to sequential processing of every MP-POV. We then categorize MP-POVs at the current scale to limited groups through predefined patterns (see Fig. 5), with which the coding efficiency is slightly compromised but the complexity is greatly saved to several orders of magnitude.

SLNE Enhanced SOPA. Previous explorations only assume the operations along with the upscaling process, in which the very straightforward dyadic voxel downscaling is used in the encoder. Here we propose the SLNE to analyze neighborhood variations for each POV, and then embed such a local relationship as its feature attribute. As for scale upscaling, because we now can use both occupancy status and feature attribute of each decoded POV, the approximation accuracy of occupancy probability can be significantly improved for One-Stage SOPA. While for Multi-Stage SOPA, the additive gain is marginal since the multi-stage processing already well utilizes the correlation across spatially-connected MP-POVs (see Table 2).

1.3 Contribution

Our contributions are summarized as follows:

- Together with the preliminary exploration in [23], we probably are the *first one* to suggest the sparse tensor processing based multiscale representation for point cloud geometry compression, a.k.a., SparsePCGC;
- The proposed SparsePCGC generalizes itself very well with the state-of-the-art efficiency in both lossless and lossy scenarios, across a variety of datasets,

TABLE 1: Notations and Abbreviations

Abbreviation	Description
PCC	Point Cloud Compression
PCG	Point Cloud Geometry
PCGC	Point Cloud Geometry Compression
POV	Positively-occupied Voxel
MP-POV	Most Probable POV
NOV	Non-Occupied Voxel
SparseCNN	Sparse Convolution based Neural Networks
SOPA	SparseCNN based Occupancy Probability Approximation
SOPA (Position)	SparseCNN based Occupancy Position Adjustment
SLNE	SparseCNN based Local Neighborhood Embedding
G-PCC	Geometry-based PCC
BD-Rate	Bjørtegaard Delta Rate [22]

such as the densely-sampled 8i Voxelized Full Bodies (8iVFB) and Owlii sequences, sparsely-sampled LiDAR sequences KITTI and Ford, in comparison to the standardized G-PCC and other learning-based approaches [8]–[10], [12], [14], [23]–[25].

- The proposed SparsePCGC also demonstrates the lightweight space and time complexity consumption. For example, its computational runtime for encoding and decoding is comparable to the G-PCC (see Table 2), and reduces the running time by orders of magnitude to recently published VoxelDNN [26] and NNOC [25]. And, applying the model sharing across scales would significantly reduce the space requirement for model storage which is attractive to industrial practitioners.

It is worth to point out that our solution is now under investigation in MPEG for the exploration of next-generation point cloud compression. Our superior coding performance is also cross-checked by third parties in standardization experiments [27]. Table 1 lists notations and abbreviations frequently used in this work for convenience.

2 RELATED WORK

This section reviews relevant techniques for PCGC, with the main focus on the learning-based solutions.

2.1 Rules-based Approaches

The octree model is the most popular format to represent voxelized point cloud [28]. Here, a volumetric point cloud is recursively divided using octree decomposition until it reaches the leaf nodes/voxels. The voxel or sub-voxel occupancy can be then statistically compressed through its entropy context modeling conditioned on neighboring nodes that are arranged using parent-child trees [29], [30]. This octree-based coding mechanism is adopted in MPEG G-PCC [31], known as the *octree geometry codec*.

To reconstruct object surfaces with finer spatial details, a number of triangle meshes are constructed locally together with the octree model [32]. MPEG G-PCC has then included such triangulation-based mesh model, a.k.a., triangle soups representation of local geometry into the test model which is known as the *trisoup geometry codec*.

Alternatively, traditional methods for 2D image and video coding have demonstrated outstanding efficiency and have been widely used in standards and products. This motivates us to project a given 3D object to multiple 2D planes from a variety of viewpoints and hence we can leverage popular image and video codecs for compact representation of point cloud. Examples include the MPEG Video-based PCC [1], View-PCC [33], etc. Such 3D-to-2D projection based solution is a different exploration route, and is not the focus of this work.

2.2 Learning-based Methods

Numerous works have shown that data-driven learning using DNNs can improve the performance of PCGC in both lossy and lossless coding scenarios significantly.

Uniform Voxel Representation. Earlier attempts, including Wang *et al.* [8], Quach *et al.* [7], and Guarda *et al.* [9] assume the uniform voxel model (see Fig. 1(a)) to represent voxelized volumetric point cloud, by which we can directly apply 3D dense convolutions to analyze and capture spatial correlations of inter voxels. These 3D CNN layers are often stacked in an autoencoder architecture with quantized latent features at bottleneck layer compressed using an adaptive arithmetic coder. For any given feature element at the bottleneck, its hyperprior and autoregressive neighbors can be utilized for its probability estimation.

Octree Representation. As in such uniform voxel representation, even for those empty voxels, e.g., NOVs, we still need to treat them equally as POVs in computation, leading to great consumption of storage and computation. Then, octree decomposition is introduced because it can utilize a tree structure to progressively represent voxels from coarse to fine scales for compact representation. Huang *et al.* [12] and Biswas *et al.* [13] adopt the Multi-Layer Perceptron (MLP) to exploit the dependency between parent and child nodes for better prediction of occupancy probability.

Hybrid Octree & Uniform Voxel. In addition to the utilization of parent-child dependency, local neighboring nodes at the same octree depth can be also converted into uniform voxel representation for context modeling using dense 3D CNNs. Such hybrid octree and uniform voxel representation is actively investigated in [14]. Although such hybrid model outperforms octree model on LiDAR data, its performance on dense PCG is unknown.

Point-wise Representation. Alternative point-wise solutions directly compress the raw points of input point cloud without voxelization. They typically apply the Point-Net++ [18] or other MLP based autoencoders. As reported in [17], point-wise approaches present lightweight complexity consumption, however the coding efficiency of these point-wise models still suffers, not only performing poorly at high bit rates, but also having difficulties to generalize themselves to large-scale point clouds.

As will be shown later, the proposed SparsePCGC can effectively solve problems in existing solutions with better coding efficiency and lower complexity. To help audience understand the proposed framework quickly, we first review sparse tensor processing below and then unfold the algorithm details step by step.

3 SPARSE TENSOR PROCESSING

3.1 Sparse Tensor

The number of occupied voxels or MP-POVs is just a few percentage of total voxels in a 3D volumetric PCG, exhibiting very sparse distribution in a space. Thus, we choose to use the *Sparse Tensor* (see Fig. 1c) to represent a voxelized PCG, with which we only cache the geometric coordinates and attributes (if applicable) of those MP-POVs for processing. It then uses a hash map to index the voxel coordinates and an auxiliary data structure to manage their connections efficiently. As such, we not only greatly reduce the complexity by just performing the computation on MP-POVs, but also can analyze and aggregate effective neighborhood correlation using sparse convolutions.

By contrast, The octree model is limited by the relationship between parent and child nodes due to the tree structure, which is difficult to represent spatial neighbors unless we explicitly construct such local spatial connections; while the uniform voxel model has to use the regular grid to store all voxels in 3D space regardless of their occupancy, which is obviously redundant. As such, the sparse tensor can represent the MP-POVs in a PCG and their internal connections more efficiently, compared to the octree and uniform voxel representation.

3.2 Sparse Convolution

The sparse tensor is designated for efficient 3D sparse convolution. It is the same as the common dense convolution in principle but only convolves at MP-POVs, which makes full use of the sparse characteristics of a point cloud.

A sparse tensor can be formulated using a set of coordinates $\vec{C} = \{(x_i, y_i, z_i)\}_i$ and associated features $\vec{F} = \{\vec{f}_i\}_i$. Thus the sparse convolution is:

$$\vec{f}_u^{out} = \sum_{k \in N^3(u, \vec{C}^{in})} W_k \vec{f}_{u+k}^{in} \quad \text{for } u \in \vec{C}^{out} \quad (2)$$

where \vec{C}^{in} and \vec{C}^{out} are input and output coordinates. \vec{C}^{in} and \vec{C}^{out} are the same if the resolution is kept. \vec{f}_u^{in} and \vec{f}_u^{out} are input and output feature vectors at coordinate u (a.k.a., (x_u, y_u, z_u)). $N^3(u, \vec{C}^{in}) = \{k | u + k \in \vec{C}^{in}, k \in N^3\}$ defines a 3D convolutional kernel centered at u with offset k in \vec{C}^{in} . By setting different k , we can easily retrieve neighboring voxels within a predefined 3D receptive field for information aggregation. W_i is kernel weights.

Clearly, the computational and space complexity is greatly reduced by the sparse convolution in comparison to the regular dense convolutions. More details regarding the sparse convolutions can be also found in [21]. As in Table 2, our sparse tensor-based solution could offer comparable complexity with the MPEG G-PCC anchor, and only requires just a few percentage of running time of those uniform voxel based methods [10], [26] (see Table 4). In the meantime, our method requires a small amount of storage due to model sharing across scales (see Sec. 7.4).

4 SPARSE TENSOR BASED MULTISCALE PCGC

This section first pictures the overall system design and then offers technical details of the proposed SparsePCGC.

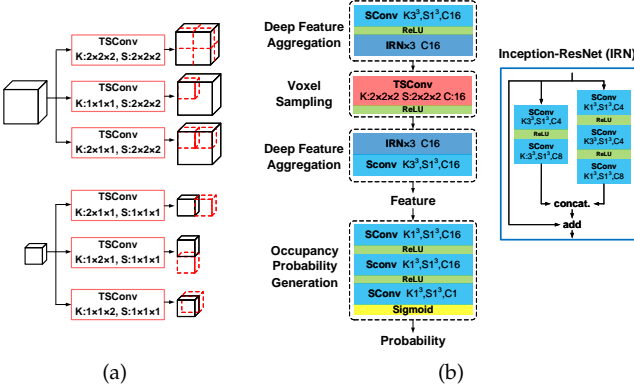


Fig. 3: **Basic SparseCNN Modules.** Illustration examples of SparseCNN used in various tasks, e.g., voxel sampling, deep feature aggregation, occupancy probability generation, etc. (a) Voxel sampling layer with different SparseCNN settings; (b) the SOPA model using stacked SparseCNN for occupancy probability approximation.

4.1 Framework

A general framework of proposed sparse tensor based multiscale PCGC is illustrated in Fig. 2. We call it SparsePCGC for short³. It includes a pair of encoder and decoder, where the encoder inputs the PCG for the generation of the compressed bitstream, and the decoder parses the bitstream to reconstruct the original PCG.

The framework contains a sequence of dyadic voxel sampling, e.g., $S : 2 \times 2 \times 2 \uparrow$ as the upscaling, or $S : 2 \times 2 \times 2 \downarrow$ as the downscaling. They can be integrated with the SparseCNN units for better resampling.

Such progressive scaling enables the multiscale representation so that we can easily support the resolution scalability. Since we enforce the identical processing between two adjacent scales, the overall SparsePCGC can be comprehensively explained through a two-scale example, such as $(i-1)$ -th scale to i -th scale as in Fig. 2.

As seen, each POV from the preceding scale will be subdivided into eight MP-POVs (see Fig. 1e), of which some may be POVs and the rest are NOVs. The ground truth is known in the encoder but is unknown in the decoder. At each scale, we need to compress the occupancy status of each MP-POV known in the encoder, and reversely reconstruct POVs from upscaled MP-POVs in decoder by interpreting compressed syntax. Thus, the same context model is shared in both encoder and decoder to estimate the occupancy probability for arithmetic coding. The cross-scale context modeling is facilitated by the SOPA to use decoded POV in preceding scale to generate p_{MP-POV} of each upscaled MP-POV.

The next section first briefs basic SparseCNN modules used in SparsePCGC.

3. Note that we exemplify ideas below using lossless PCGC, while as will be reported later, the proposed architecture can be easily extended to support lossy PCGC. Our preliminary exploration on lossy PCGC can be found in [23].

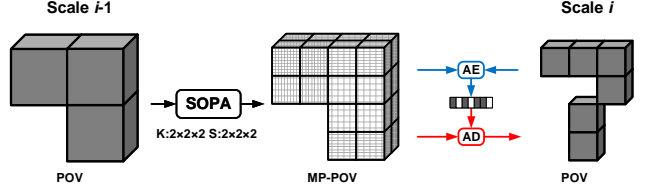


Fig. 4: **One-Stage SOPA.** Each decoded POV is processed by the SOPA engine to generate eight MP-POVs and associated PMP-POVs. The encoder uses p_{MP-POV} to encode ground truth into binary stream while the decoder determines true POVs and NOVs by decoding binary stream with $p_{MP-POVs}$.

4.2 Basic SparseCNN Architecture

The SparseCNN generally stacks layers for deep feature aggregation, voxel sampling, occupancy probability generation shown in Fig. 3. All of these computations are operated on sparse tensor.

Voxel Sampling Layer. We embed voxel upscaling in SOPA and voxel downscaling in SLNE⁴ to execute the cross-scale message passing (see red painted voxel sampling layer in Fig. 3b and Fig. 7a).

For the downscaling in SLNE shown in Fig. 7a, we apply the Sparse Convolution (SConv) with the Kernel (K) and Stride (S) size of $2 \times 2 \times 2$ to merge the voxels in every $2 \times 2 \times 2$ space into a single voxel. Oppositely, for the upscaling in SOPA shown in Fig. 3b, we apply the Transposed Sparse Convolution (TSCNN) with $K : 2 \times 2 \times 2$ and $S : 2 \times 2 \times 2$ ⁵ to sub-divide a voxel into eight sub-voxels.

As shown later for Multi-Stage SOPA, we can devise asymmetric TSCNN to approximate grouped p_{MP-POV} from one to another, by which we can step-wisely exploit interdependency of neighboring MP-POVs for better accuracy. As in Fig 3b, we list six different TSCNN settings with various kernel sizes and strides. For example, $TSCNN = \{K : 2 \times 1 \times 1, S : 2 \times 2 \times 2\}$ will upscale the resolution in x -, y - and z - axis by a factor of 2, but only generate two new sub-voxels in x -axis, while $TSCNN = \{K : 2 \times 1 \times 1,$

4. If we do not include the SLNE in encoder, simple dyadic voxel downscaling is used.

5. We can also use $K2^3$ and $S2^3$ for simple notation. We omit the \uparrow and \downarrow by implicitly implying the voxel upscaling and downscaling using respective TSCNN and SConv.

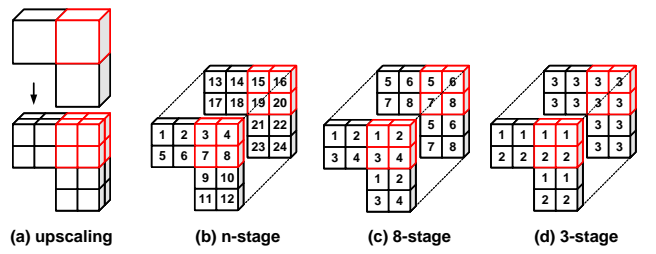


Fig. 5: **Grouping Strategies.** (a) Upscaling each decoded POV to eight spatially-connected MP-POVs; (b) n -Stage SOPA using one-by-one sequential processing; (c) 8-Stage SOPA by classifying eight MP-POVs upscaled from the same POV into 8 groups; (d) 3-Stage SOPA by grouping eight MP-POVs upscaled from the same POV into 3 groups.

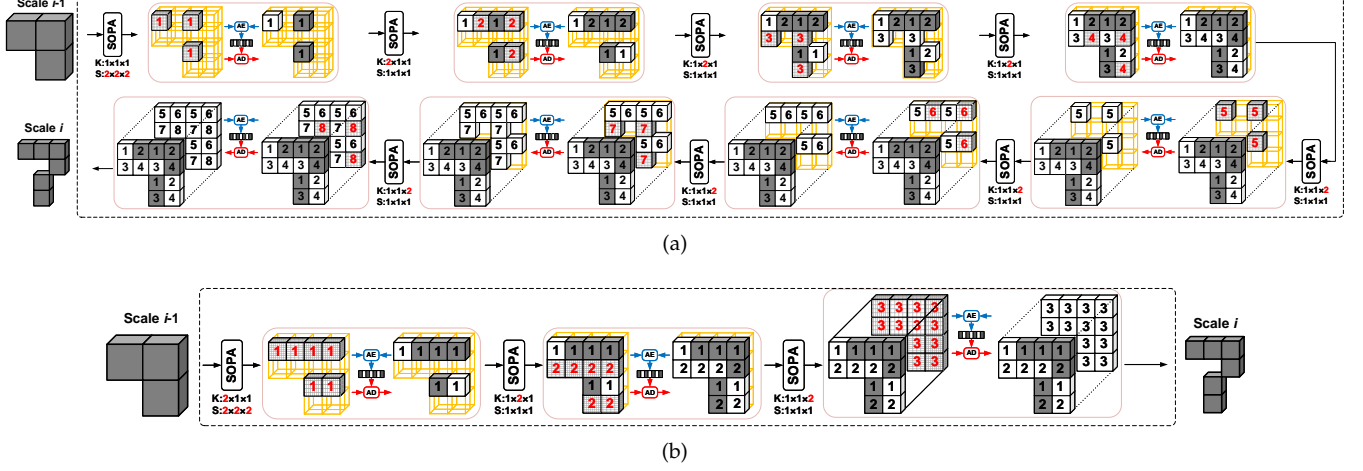


Fig. 6: **MultiStage SOPA.** (a) 8-Stage SOPA. (b) 3-Stage SOPA. Boxes with dense grid pattern and red numbers are MP-POVs (and their probabilities) just upscaled from last scale; Solid grey and white boxes with black numbers are respective POVs and NOVs identified by parsing the bitstream which are then used for next-stage MP-POV derivation. AE and AD are arithmetic encoding and decoding.

$S : 1 \times 1 \times 1\}$ will maintain the same resolution but generate a new voxel in x -axis. Ideally, we can adaptively generate new voxels by setting different parameters of K and S of asymmetric TSConv, e.g., $\{K : k_x \times k_y \times k_z, S : s_x \times s_y \times s_z\}$.

Deep Feature Aggregation. For most convolutional layers, we typically use SConv = $\{K : 3 \times 3 \times 3, S : 1 \times 1 \times 1\}$ to aggregate feature of neighboring voxels at the same scale. Long-range information aggregation can be enabled by stacking deep convolutional layers. In practice, we apply a deep Inception Residual Network (IRN) block that is comprised of three basic IRN units [34], before and after the voxel sampling layer separately to better characterize the spatial dependency across neighborhood voxels. The IRN is also used in our earlier attempts [8], [23].

As for the One-Stage SOPA in Fig. 3b, the probability generation module is placed in the last step, which consists of three convolutional layers and a sigmoid activation layer to derive the occupancy probability p in the range of $[0,1]$.

4.3 Lossless SOPA: Exploiting Spatial Priors For More Compact Representation

The compression performance of SparsePCGC is mainly determined by the efficiency of the SOPA engine for context modeling. Even for SLNE, it is also utilized to improve the SOPA for a more accurate entropy probability approximation. We start our discussion from a toy baseline.

4.3.1 A Toy Baseline Using One-Stage SOPA Only

This example only allows dyadic voxel downscaling (e.g., no SLNEs in encoder) for encoding, and ultimately relies on the One-Stage SOPA engine for one-shot $p_{\text{MP-POV}}$ estimation. As shown in Fig. 4, it basically inputs the occupancy status of each POV from preceding scale to generate $p_{\text{MP-POVs}}$ of corresponding upscaled 8 MP-POVs. It applies the TSConv = $\{K : 2 \times 2 \times 2, S : 2 \times 2 \times 2\}$ in voxel sampling layer for upscaling. In fact, we can barely learn sufficient information by only using the binary occupancy status for $p_{\text{MP-POV}}$ estimation in such a one-shot manner, leading to inferior coding efficiency to the G-PCC anchor (see Table 2).

4.3.2 Multi-Stage SOPA

Previous One-Stage SOPA assumes that eight MP-POVs upscaled from a POV of last scale are independent of each other. Whereas, they are closely correlated because they are generated from the same POV and are present in close proximity. Hence this section develops the Multi-Stage SOPA to step-wisely estimate the $p_{\text{MP-POV}}$ in upscaled sparse tensor from one group to another by exploiting the dependency among MP-POV neighbors. Leveraging neighboring MP-POVs for more accurate $p_{\text{MP-POV}}$ estimation is also referred to as the utilization of autoregressive priors that have been extensively used for image/video coding [11], [36].

Hereafter, the Multi-Stage SOPA is mainly about how to group upscaled MP-POVs and how to exploit inter-group dependency. We have exemplified three typical grouping strategies in Fig. 5. The same methodology can be easily extended to other grouping schemes.

n -Stage SOPA. One special case is to process all MP-POVs one by one regardless of the diverse POVs they are upscaled from. Given that 3D masked CNN is an efficient method for such sequential computation, we propose to first use TSConv = $\{K : 2 \times 2 \times 2, S : 2 \times 2 \times 2\}$ to upscale all decoded POVs, and then apply 3D masked CNNs to derive $p_{\text{MP-POV}}$ one by one from top to bottom, from left to right, and from front to back. This lets us use the occupancy information of the past and causal neighbors to estimate $p_{\text{MP-POV}}$ of current MP-POV.

Although we do not strictly follow the SOPA architecture for this special case, we would like to call it “ n -Stage SOPA” for consistent terminology. Unfortunately, such “ n -Stage SOPA” suffers from an extremely long duration for decoding due to sequential computation, e.g., ≈ 1 hour averaged for 8iVFB test samples, making it impractical for applications.

Recalling that we actually upscale each POV of preceding scale to a corresponding “8 MP-POVs” set of current scale, we suggest to properly group these eight MP-POVs of a “8 MP-POVs” set, and apply the same grouping strategy to all other “8 MP-POVs” sets. This allows us to not only ex-

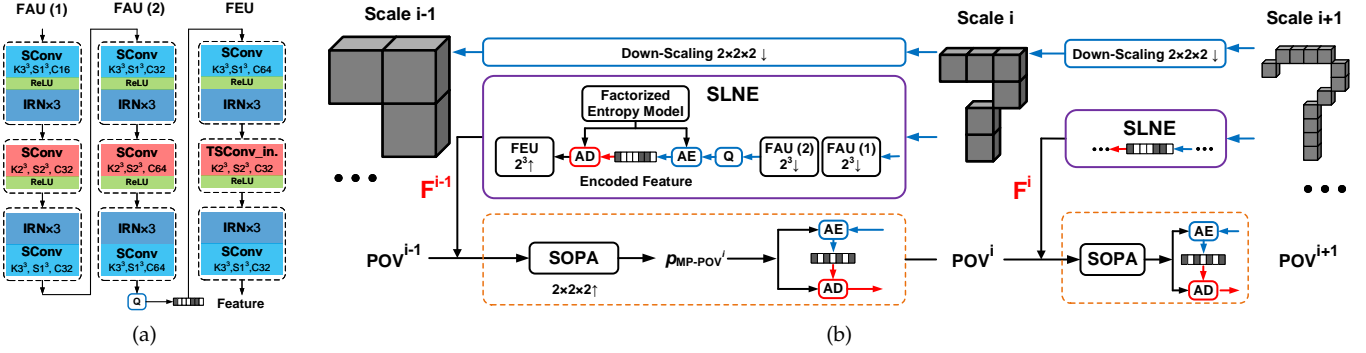


Fig. 7: **SLNE enhanced One-Stage SOPA.** (a) the SLNE model with two FAUs (Feature Aggregation Unit) for feature downscaling and one FEU (Feature Expansion Unit) for upscaling. Quantization (Q) that is widely used in learnt image/video coding [11], [35] is applied where the uniform noise injection is used in training and rounding is used in inference. The factorized entropy model is used for feature context modeling [35]. (b) SLNE enhanced One-Stage SOPA exemplified in a two-scale architecture. At each scale, the occupancy status and feature attribute of the sparse tensor are separately encoded and multiplexed in binary stream.

ploit the close dependency within spatially-connected MP-POVs, but also massively speed up the processing time by several orders of magnitude, since all MP-POVs belonging to the same group can be processed concurrently.

8-Stage SOPA. For any given “8 MP-POVs” set at a certain scale, an intuitive solution is to categorize each element into an individual group, resulting in eight groups in total shown in Fig. 5c. The same grouping is applied to all “8 MP-POVs” sets. Therefore, all MP-POVs at the current scale that are labeled with “1”, e.g., 1st-group MP-POVs, will be processed simultaneously at first, and then MP-POVs labelled with “2” (a.k.a., 2nd-group MP-POVs), till we traverse all eight groups. Note that we can use the occupancy status of previously-proceed MP-POVs to assist the processing of succeeding MP-POVs, with which we significantly improve the SOPA efficiency in the next steps.

Figure 6a details the 8-Stage SOPA step by step. We first generate $p_{\text{MP-POVs}}$ for 1st-group MP-POVs (see dense grid box) by applying the $\text{TSConv} = \{K : 1 \times 1 \times 1, S : 2 \times 2 \times 2\}$ in voxel sampling layer of a SOPA module. These $p_{\text{MP-POVs}}$ s are used in encoding thread to compress the ground truth of 1st-group, and in decoding thread to parse incoming bitstream to identify POVs and NOVs in 1st-group MP-POVs (see grey POVs and white NOVs labeled with same “1”).

We further derive $p_{\text{MP-POVs}}$ for 2nd-group MP-POVs by using the $\text{TSConv} = \{K : 2 \times 1 \times 1, S : 1 \times 1 \times 1\}$ with the full knowledge of POVs in 1st-group MP-POVs. The similar process continues till we complete all groups. The knowledge of POVs from last stages will be used as priors for improving the probability estimation in next steps.

For simplicity, we use the asymmetric TSConv by only convoluting one spatially-connected neighbor. For example, 3rd- and 4th-group MP-POVs are generated with the help of their respective y -axis neighbor, i.e., previously-processed 1st- and 2nd-group MP-POVs. Similarly, MP-POVs from the 5th to the 8th groups are generated by utilizing their z -axis neighbors from the 1st to the 4th groups respectively.

3-Stage SOPA. In order to further balance the coding efficiency and complexity, we simplify this 8-Stage SOPA

to a 3-Stage SOPA solution, in which we basically process the MP-POVs line-by-line. For example, we can group MP-POVs with “1” and “2” labels together as the 1st group, unite MP-POVs labelled with “3” and “4” as the 2nd group, and finally cluster “5”, “6”, “7”, “8” labelled MP-POVs altogether as the 3rd group, as illustrated from Fig. 5c to Fig. 5d. As in Fig. 6b, we have devised the voxel sampling layers with $\text{TSConv} = \{K : 2 \times 1 \times 1, S : 2 \times 2 \times 2\}$ for generating 1st-group MP-POVs, $\text{TSConv} = \{K : 1 \times 2 \times 1, S : 1 \times 1 \times 1\}$ for the 2nd group, and $\text{TSConv} = \{K : 1 \times 1 \times 2, S : 1 \times 1 \times 1\}$ for the 3rd group, in each SOPA step by step.

For either Multi-Stage or One-Stage SOPA, we can approximate the bit rate of MP-POV occupancy status at $(i-1)$ -th scale using

$$R_s(i) = \sum_k -\log_2(p_{\text{MP-POV}}^{i-1}(k)). \quad (3)$$

$p_{\text{MP-POV}}^{i-1}(k)$ is occupancy probability of k -th MP-POV at $(i-1)$ -th scale derived using priors from preceding scale or stages.

By far, the SOPA model only uses the occupancy status of POVs from either preceding scale or last stages for approximating the remaining $p_{\text{MP-POVs}}$. Next section will discuss potentials to learn and embed spatial priors as the feature attribute in encoder for improving the SOPA efficiency.

4.3.3 SLNE Enhanced SOPA

Since we know ground-truth labels at each scale in the encoder, we further see whether we can learn and embed local spatial variations as feature attribute. In this case, for each POV, besides its occupancy status signaling, we have such neighborhood variation feature that will be compressed and decoded to enhance the capacity of the SOPA engine. This section exemplifies the SLNE-enhanced One-Stage SOPA. Other combinations can be easily extended.

Figure 7 exemplifies the SLNE between i -th and $(i-1)$ -th scales. Similar to the SOPA model, the same SLNE is applied to any two adjacent scales. As seen, in addition to geometrically downscale the sparse tensor \mathbf{POV}^i to the

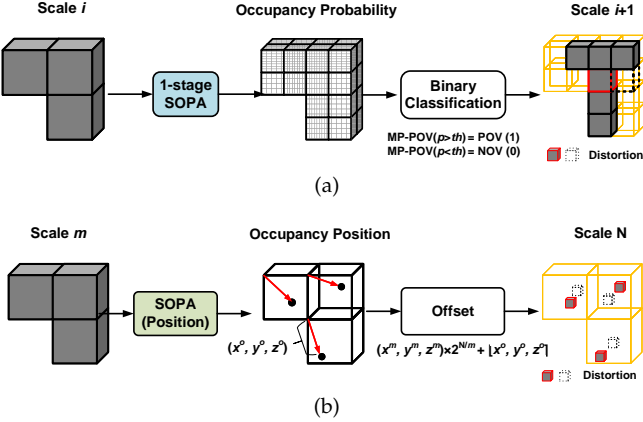


Fig. 8: **Lossy SOPA.** (a) Probability thresholding for dense point clouds; (b) Position offset adjustment for sparse LiDAR point clouds.

POV^{i-1} , the SLNE aggregates local neighborhood variations for each POV as its feature attributes \mathbf{F}^{i-1} . Thus, both occupancy status and feature attributes of each POV in POV^{i-1} are compressed into the binary stream, where the rate of occupancy status uses (3), and the rate of lossy coded feature attributes is

$$R_f^{i-1} = \sum_k -\log_2(p_{\mathbf{F}^{i-1}}(k)). \quad (4)$$

having the $p_{\mathbf{F}^{i-1}}$ follow the factorized entropy model [35] with its parameters determined in training.

From the decoding point of view, both reconstructed occupancy status and features of each POV at $(i-1)$ -th scale are fed into the SOPA engine to derive the probabilities of MP-POVs at i -th scale for subsequent processing. The occupancy reconstruction is achieved by decoding the occupancy status related bitstream using estimated MP-POV probabilities; while the feature reconstruction applies the Feature Expansion Unit (FEU) to upscale decoded features by a factor of 2 in three-dimensional axis accordingly.

Note that the feature attribute processing, e.g., downscaling, encoding, decoding, and upscaling, are contained within two consecutive scales (see Fig. 7b). Applying two consecutive Feature Aggregation Units (FAUs) before quantization (see Fig. 7a) could well balance the compactness and efficiency of quantized features for optimally estimating the MP-POV probability in i -th scale tensor according to our extensive simulations. Having one FEU to upscale decoded features is to match the geometry resolution of the sparse tensor that is upscaled for next-scale MP-POV derivation.

5 UNIFIED LOSSLESS AND LOSSY COMPRESSION

Past sections detail the SOPA variants in lossless mode. Here, we show that it can be easily extended to support the lossy compression under a unified model. A slight modification is that we apply different strategies in the lossy SOPA engine for dense and sparse point clouds to reflect their very different characteristics.

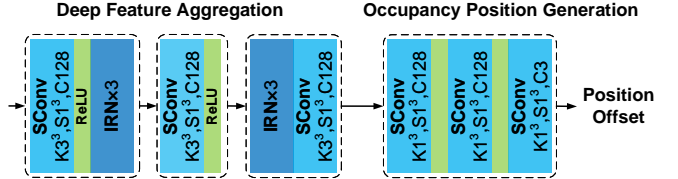


Fig. 9: **SOPA (Position).** Voxel sampling layer of original SOPA in Fig. 3b is replaced by the SConv = { K : $3 \times 3 \times 3$, S : $1 \times 1 \times 1$ }, and the occupancy probability generation module is substituted by the occupancy position generation for offset derivation.

5.1 Lossy SOPA

5.1.1 Probability Thresholding for Dense Point Clouds

Recalling that we apply the occupancy probability generation in SOPA shown in Fig. 3b to exactly derive the probability of each MP-POV in lossless mode, the lossy mode is simply using the probability threshold th to classify the binary occupancy status, e.g., the MP-POV is a POV, if $p_{MP\text{-POV}} > th$, otherwise it is a NOV, as in Fig. 8a. th is set adaptively according to the number of POVs at the current scale, which is the same as our previous works [8], [23]. Apparently, distortion is inevitably introduced due to false classification.

For the Multi-Stage SOPA model in Fig. 6, the probability estimation in the succeeding step relies on the outcome of preceding stages, which means that a false classification in lossy mode may lead to unexpected results. Thus, we choose the One-Stage SOPA for lossy compression.

5.1.2 Position Offset Adjustment for Sparse Point Clouds

The aforementioned probability thresholding-based lossy SOPA works well for dense point clouds. However, it fails for sparse point clouds, particularly for higher scales, because the point distribution is extremely sparse and random, for which occupancy estimation of the MP-POV is inefficient.

Thus the occupancy *probability approximation* in the native SOPA model is replaced by occupancy *position adjustment*. For clarification, we then referred it to as the “SOPA (Position)” shown in Fig. 8b.

The SOPA (Position) model in Fig. 9 shares almost the same architecture as the native SOPA model in Fig. 3b. But, the voxel sampling layer is replaced by a SConv = { K : $3 \times 3 \times 3$, S : $1 \times 1 \times 1$ }, and the channels of intermediate layers are increased to 128. The triple-channel output layer is used to produce the position offset for adjustment.

Since we directly estimate the position offset, it does not require to do dyadic scaling progressively. Thus, for the input m -th scale sparse tensor, we upscale it to N -th scale in one-shot ($N > m$) as in Fig. 8b. For a given POV at (x^m, y^m, z^m) in m -th scale tensor, its corresponding POV at N -th scale locates at

$$(\hat{x}^N, \hat{y}^N, \hat{z}^N) = (x^m, y^m, z^m) \times 2^{\frac{N}{m}} + [x^o, y^o, z^o], \quad (5)$$

with (x^o, y^o, z^o) as the position offset estimated from SOPA (Position).

Though position adjustment expands the resolution, it does not increase the number of POVs which well reflect

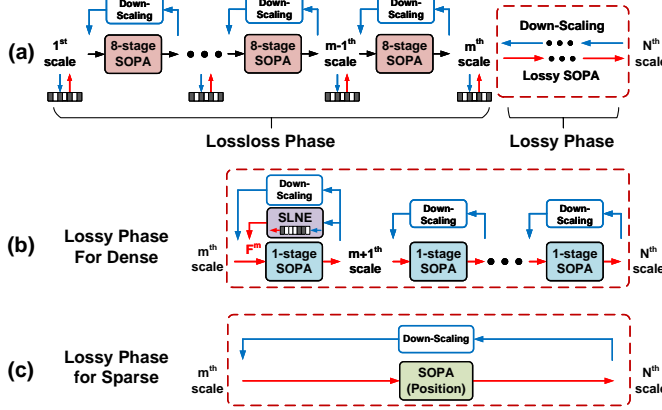


Fig. 10: **Lossy SparsePCGC**. (a) General architecture with m scales coded losslessly and $(N - m)$ scales coded in lossy mode; (b) lossy SOPA for dense point clouds; (b) SOPA (Position) for sparse point clouds;

the sparsity nature of LiDAR sequences observed by our analysis on the characteristics of sparse clouds. Similar position adjustment methodology is also found in [14] to encode sparse point clouds, where it is called “coordinates refinement”.

5.2 Unified SparsePCGC Framework

Previous discussions focus on the development of models using two adjacent scales in either lossy or lossless mode. In practice, the SparsePCGC stacks a sequence of two-scale models to process either dense or sparse PCG, in either lossy or lossless option.

In lossless mode, the solution is fairly straightforward, in which we apply lossless SOPA models to compress both dense and sparse PCGs across all scales. The compression ratio against the G-PCC anchor is used to evaluate the performance of the proposed SparsePCGC.

In lossy mode of Fig. 10, the SparsePCGC devises the lossless coding from the first to m -th scale, and the lossy mode to remaining scales. Adapting m is to best balance the rate and distortion for lossy compression. As reported in [23], having lossy coded PCG for all scales would produce severe degradation of reconstruction quality due to scale-by-scale refinement, but could not bring noticeable rate reductions.

Note that the highest scale N is typically determined by the geometry precision of input point clouds. For example, $N = 10$, or 11 for dense 8iVFB and OwlII, and $N = 18$ for KITTI and Ford sequences.

6 TRAINING

This section details the datasets, loss functions, and strategies used in training.

6.1 Datasets

We select the ShapeNet [37] and KITTI [38] that are publicly accessible as two typical training datasets for dense and sparse point clouds.

- **ShapeNet** [37] is one of the most popular CAD model datasets for 3D objects. Its subset ShapeNet-Core contains 55 common object categories with about 51,300 unique 3D mesh models. We densely sample points on raw meshes to generate point clouds, and then randomly rotated and quantized them with 8-bit geometry precision at each dimension.

- **KITTI** (SemanticKITTI) [38] is a large-scale LiDAR dataset used for semantic scene understanding. It contains 22 sequences, a total of 43,552 scans of outdoor scenes collected using the Velodyne HDL-64E LiDAR sensor. There are around 120k points on average per frame. These raw floating-point coordinates are quantized to millimeter scale (e.g., 1mm as unit precision), requiring 18-bit geometry precision for storage.

Data Augmentation. In practice, the characteristics of point clouds vary greatly from one to another. Among them, geometry precision is one of the most important factors, because it has a significant impact on the spatial variance, density, and thus the compression efficiency of point clouds.

It is impractical to assume a fixed geometry precision for raw input and it is also difficult to set a constant number of scales. Recalling that our solution applies the resolution scaling for multiscale representation, we suggest training the models used for two consecutive scales, and then directly applying them for inference in a multiscale manner, i.e., all models share all the same weights across scales. This makes our solution attractive to practical applications because of its lightweight complexity requirement.

In order to generalize the trained models to an excessive content, we first downscale the point clouds by a random scaling factor in $[0.5, 1)$, and then perform dyadic voxel downscaling upon them with the scaling factors at $\{1, \frac{1}{2}, \frac{1}{4}, \frac{1}{8}, \dots\}$ to obtain ground-truth labels at multiple scales. These ground-truth labels are then used to supervise the training of SOPA and SLNE models.

6.2 Loss Functions

Basically, the SOPA model estimates the probability of occupancy status $p_{MP\text{-}POV}$ for a given MP-POV at a specific scale, which is then used to code binary occupancy symbol of this MP-POV in lossless mode, and to perform the binary classification in lossy compression mode.

In general, the Binary Cross-Entropy (BCE) between estimated occupancy probability and real occupancy symbol is used in training, i.e.,

$$L_{BCE} = \sum_k -(o(k) \log_2(p(k)) + (1 - o(k)) \log_2(1 - p(k))), \quad (6)$$

where $o(k)$ represents the real occupancy symbol (1 for POV or 0 for NOV), $p = p_{MP\text{-}POV}$ is the probability that this k -th MP-POV is POV, and thus $(1-p)$ is the probability of being the NOV.

Note that the SOPA model can be improved by the inclusion of SLNE model in the encoding process. Thus, the loss



Fig. 11: **Point Cloud Examples.** (a) dense point clouds 8iVFB; (b) Sparse LiDAR point clouds KITTI.

function for SLNE enhanced SOPA models is combining the BCE loss in (6) and rate consumption for feature attributes:

$$L_{\text{comb}} = L_{\text{BCE}} + R_F, \quad (7)$$

with R_F defined in (4).

For sparse point clouds using SOPA (Position), we treat it slightly different. Given that the SOPA (Position) model directly outputs the occupancy position offset, we suggest to measure the Mean Square Error (MSE) between the coordinates of adjusted points and true points in upscaled tensor, i.e.,

$$L_{\text{MSE}} = \sum_k ((x^N, y^N, z^N)(k) - (\hat{x}^N, \hat{y}^N, \hat{z}^N)(k))^2, \quad (8)$$

6.3 Training Strategies

Overall, the training of SOPA models is very straightforward and easy to do. The SLNE enhanced Single-Stage SOPA model is slightly difficult to train because of the combined loss used in SLNE. Therefore we propose to set the weight of R_F to 0 in (7) at first, and then gradually increase it to 1 in training for robust and fast converge. For SLNE enhanced Multi-Stage SOPA, only the SOPA models are updated, while the SLNE model is directly borrowed from the SLNE enhanced Single-Stage model and its parameters are fixed in training.

The learning rate decreases from 0.0008 to 0.00002 in the training. The training iteration executes around 30 epochs with a batch size of 8. Adam is used as the optimizer.

7 EXPERIMENTAL STUDIES

7.1 Test Setup

Datasets. The MPEG PCC datasets [39] that are recommended and used by standardization committee are tested for performance evaluation.

Dense Point Clouds. We choose several static samples from the Category 1 of MPEG PCC dataset, including longdress_vox10_1300, redandblack_vox10_1550, soldier_vox10_0690, loot_vox10_1200, queen_0200, basketball_player_vox11_0200, and dancer_vox11_0001. They are densely sampled but have different geometric precision and characteristics to represent diverse objects.

Sparse Point Clouds. We use KITTI and Ford samples as typical sparse LiDAR point clouds. For KITTI content, we use 0-11 sequences for training (see Sec. 6.1) and 12-21 sequences for testing⁶. The raw floating-point coordinates are

⁶. Such training and testing sequence separation was commonly used in [12], [14]

quantized to 1mm (18bit required) and 2cm (13bit required) precision.

The Ford dataset is used to test dynamic acquisition point clouds as the Category 3 sample in MPEG PCC datasets. It contains 3 sequences (Ford_01, Ford_02, and Ford_03), and each sequence has 1500 frames and averaged 100k points per frame. We use all 3 sequences for testing. The original Ford dataset is already quantized to 1mm (18bit required) precision. Here, we further quantize it to 2cm (14bit required) precision for an additional test.

More information regarding the MPEG PCC datasets can be found in details in [39].

Test Conditions. For a fair comparison, we closely follow the common test conditions (CTC) [40] to generate the MPEG G-PCC anchors [41]. The latest TMC13-v14 [42] is used, and the G-PCC octree codec option is enabled for the same anchor basis in the comparative study. The angular coding mode is disabled when compressing the LiDAR point clouds based on the assumption that we do not utilize any prior knowledge from the point cloud acquisition stage. For the lossless mode of G-PCC, the “positionQuantization-Scale” is set to 1, while for the lossy compression mode, it is set to 1/2, 1/4, 1/8, etc., for variable bit rates. When evaluating the distortion for lossy compression, both *point-to-point error* (D1) and *point-to-plane error* (D2) are used to derive the PSNR. For lossless compression, the *bits per point* (bpp) is used to measure the compression ratio.

Our prototype is implemented using PyTorch and MinkowskiEngine [43], which is tested on a computer with an Intel Xeon 6226R CPU and an Nvidia GeForce RTX 3090 GPU. We record the encoding and decoding time following the methodology used in G-PCC. Because of the platform diversity, e.g., CPU vs. GPU, Python vs. C/C++, etc, the running time comparison only serves as the intuitive reference to have a general idea about the computational complexity.

7.2 SparsePCGC Presets

The SparsePCGC offers a variety of options to compress the input PCG by applying different settings of SOPA and SLNE models. This section exemplifies the typical configuration for subsequent performance evaluation and comparison.

7.2.1 Lossless Mode

For either dense or sparse point clouds, the SparsePCGC applies the lossless mode for all scales to mandate the perfect reconstruction. For simplicity, we exemplify the trade-off between the model complexity and compression efficiency by encoding dense point clouds in Table 2.

When we do not use the the SLNE function in encoder, the coding gain over the G-PCC anchor increases greatly from the toy baseline using One-Stage SOPA model, e.g., 6.6% loss, to the case using n -Stage SOPA engine, e.g., 38.7% gain. This is because the n -Stage SOPA can massively exploit autoregressive neighbors at the current scale for improving the estimation of $p_{\text{MP-POV}}$. However, the decoding time of the n -Stage SOPA is unbearable, e.g., ≈ 1 hr, due to the sequential computation from one voxel to another.

For a better tradeoff between the complexity and performance, we then devise 3-Stage and 8-Stage SOPA models. Though the coding efficiency is slightly degraded, the

TABLE 2: Compression performance and complexity (running time) tradeoff for various SOPA models in lossless mode using 8iVFB samples.

PCGs	G-PCC	One-Stage	3-Stage	8-Stage	n -Stage	SLNE Enh. One-Stage	SLNE Enh. 3-Stage
longdress_vox10_1300	1.02	1.09	0.71	0.66	0.62	0.78	0.69
redandblack_vox10_1550	1.10	1.16	0.79	0.74	0.69	0.88	0.78
soldier_vox10_0690	1.03	1.09	0.72	0.67	0.62	0.79	0.70
loot_vox10_1200	0.97	1.04	0.68	0.63	0.59	0.74	0.66
Avg. Bpp	1.03	1.10	0.72	0.68	0.63	0.80	0.71
Avg. Gain	-	+6.6%	-29.6%	-34.3%	-38.7%	-22.5%	-31.3%
Enc. Time (s)	4.0	1.6	2.2	9.5	1.6	1.6	3.0
Dec. Time (s)	1.0	1.6	2.0	9.1	$\approx 1\text{hr}$	1.6	2.5

TABLE 3: Quantitative performance gains to the G-PCC anchor. BD-Rate measurement is used for lossy mode and bits per point (bpp) is used for compression ratio comparison in lossless mode.

Point Clouds		Lossless			Lossy	
		G-PCC (bpp)	Ours (bpp)	Gain	D1-BDBR	D2-BDBR
Dense	longdress_vox10_1300	1.02	0.66	-34.8%	-93.6%	-87.3%
	red&black_vox10_1550	1.10	0.74	-33.0%	-93.5%	-87.2%
	soldier_vox10_0690	1.03	0.68	-34.4%	-93.6%	-87.4%
	loot_vox10_1200	0.97	0.63	-34.7%	-94.5%	-88.8%
	queen_vox10_0200	0.77	0.59	-23.8%	-94.2%	-88.8%
	player_vox11_0200	0.90	0.53	-40.8%	-96.7%	-93.5%
	dancer_vox11_0001	0.88	0.53	-39.7%	-96.1%	-91.9%
	Average	0.95	0.62	-34.5%	-94.6%	-89.3%
Sparse	KITTI_vox2cm	7.63	7.05	-7.5%	-23.2%	-31.0%
	Ford_vox2cm	9.95	9.64	-3.1%	-23.6%	-32.6%
	KITTI_vox1mm	20.17	19.62	-2.7%	-15.4%	-19.7%
	Ford_vox1mm	22.31	22.18	-0.6%	-12.7%	-16.6%
Average		15.01	14.62	-3.5%	-18.7%	-25.0%

decoding time is reduced by several orders of magnitudes (e.g., from one hour to several seconds). Especially, the 3-Stage SOPA costs comparable running time to the anchor.

We then explore the potentials to use SLNE in the encoder to aggregate spatial features for an even better SOPA model. Having the SLNE combined with the One-Stage SOPA, the coding efficiency is boosted from the original 6.6% loss to 22.5% gain. The coding gains can be further enlarged to 31.3% when we combine the SLNE with 3-Stage SOPA, but the relative improvement from the case only using the 3-Stage SOPA is limited (e.g., less than 2% from 29.6% to 31.3%). Such relative improvement is even negligible when we use the SLNE with 8-Stage SOPA. This is because, essentially, the SLNE and multi-stage SOPA apply the similar mechanism to exploit the local neighborhood correlation. As seen, either “SLNE enhanced One-Stage SOPA” or “SLNE enhanced 3-Stage SOPA” presents similar complexity as the G-PCC anchor, making it promising for practical implementation.

Both 8-Stage SOPA and SLNE enhanced 3-Stage SOPA are candidates for lossless SparsePCGC because of their well balanced complexity and performance. On the other hand, our simulations show that the SLNE does not work well for sparse LiDAR sequences because it is difficult to aggregate valid neighbors for efficient neighborhood embedding due to extremely sparse point distribution. Thus, “8-Stage SOPA” is suggested to losslessly encode any given PCGs.

7.2.2 Lossy Mode

As in Fig. 10, for lossless phase, we directly apply the 8-Stage SOPA model to exploit cross-scale and multi-stage correlations; while in lossy phase, we use different methods for dense and sparse point clouds due to their diverse geometry precision and relevant voxel density.

- For dense PCG, we suggest the SLNE-enhanced One-Stage SOPA to upscale sparse tensor from m -th to $(m+1)$ -th scale, and then apply the One-Stage SOPA from $(m+1)$ till the highest scale N ;
- For sparse PCG, we apply the SOPA (Position) model to directly upscale m -th scale sparse tensor to its highest scale N ;

Recalling that m is adapted for various rate-distortion trade-off of lossy SparsePCGC, in our experiments, we set the factor m as $\{N-1, N-2, N-3\}$ for dense point clouds, and $\{N-2, N-3, \dots, N-8\}$ for sparse LiDAR point clouds.

7.3 Performance Evaluation and Comparison

7.3.1 Comparison to G-PCC

We first report the performance gains of the proposed SparsePCGC to the standardized G-PCC anchor in Table 3.

Lossless Mode. For dense point clouds, our SparsePCGC improves the G-PCC by averaged 34.5% gains, and up to 40.8% gain for basketball_player_vox11_0200. For sparse point clouds, our method still outperforms the G-PCC although the gains are not as high as that for dense point

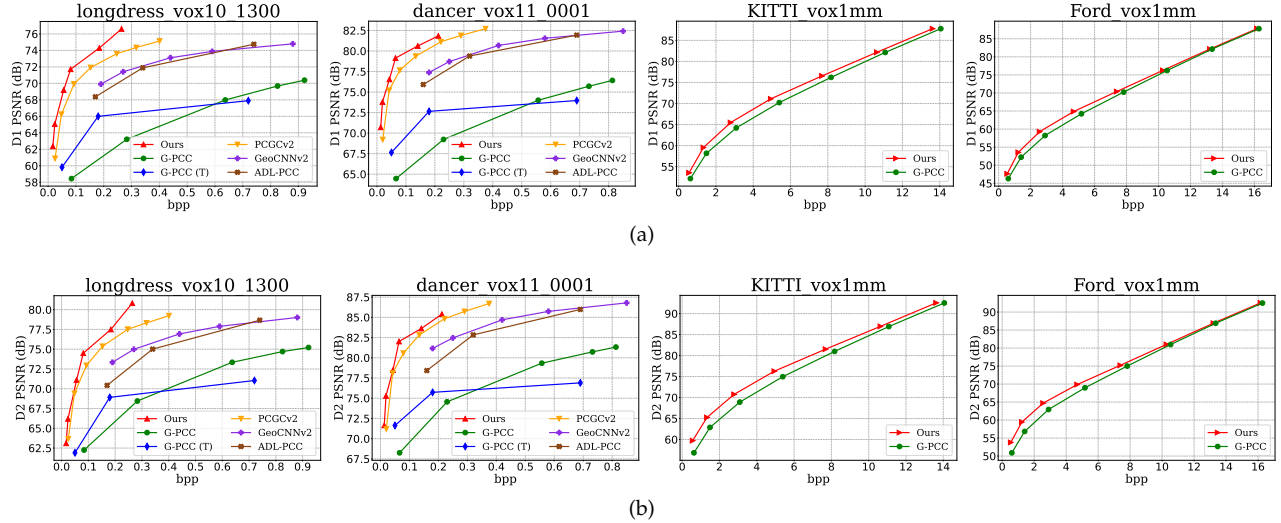


Fig. 12: Performance comparison using rate-distortion curves. (a) D1 PSNR; (b) D2 PSNR. Besides the G-PCC anchor, for dense point clouds, G-PCC (T) using trisoup codec, PCGCv2 [23], GeoCNNv2 [24], and ADL-PCC [9] are also used;

clouds. This is because sparse point clouds exhibit very sparse data distribution that is difficult to capture.

Lossy Mode. We also evaluate the lossy compression efficiency of our SparsePCGC to the anchor. On average, the proposed SparsePCGC shows 94.6% and 89.3% BD-Rate improvement for dense PCGs and 18.7% and 25.0% gains for sparse PCGs, when the distortion is respectively measured by D1 and D2 metrics. Quantitative gains to G-PCC anchor are also visualized in Fig. 12 using rate-distortion curves. Qualitative comparisons with G-PCC are presented in Fig. 13, using point clouds colored by reconstruction error.

7.3.2 Comparison to Learning-based Solutions

Most learnt approaches can only deal with a single type of point cloud. Thus, we detail the comparison individually.

Lossless Compression of Dense PCGs. Nguyen *et al.* [26] developed a learnt lossless compression method for dense PCG, termed as the VoxelDNN, in which masked 3D CNN is applied for voxel occupancy probability approximation in a uniform voxel representation. The VoxelDNN provided promising compression ratios at the expense of a very long encoding and decoding time duration incurred by the sequential processing. A multiscale parallel version of VoxelDNN, referred to as the MsVoxelDNN [10], was then extended to speed up the running time (e.g., 12x for decoding, and 16x for encoding).

In contrast to the uniform voxel representation, Kaya *et al.* [25] proposed an octree-based lossless compression method — NNOC, in which it estimates the occupancy probability of octree node based on available nodes surrounding it. Similarly, the NNOC also suffered from an extremely long encoding/decoding time. And, a fast version of NNOC, a.k.a., fNNOC, was later updated for decoding acceleration (e.g., 10x).

Table 4 compares the lossless compression efficiency of the proposed SparsePCGC, VoxelDNN (MsVoxelDNN), and NNOC (fNNOC). We run our method on the common test sequences in 8iVFB dataset used by them for a fair compar-

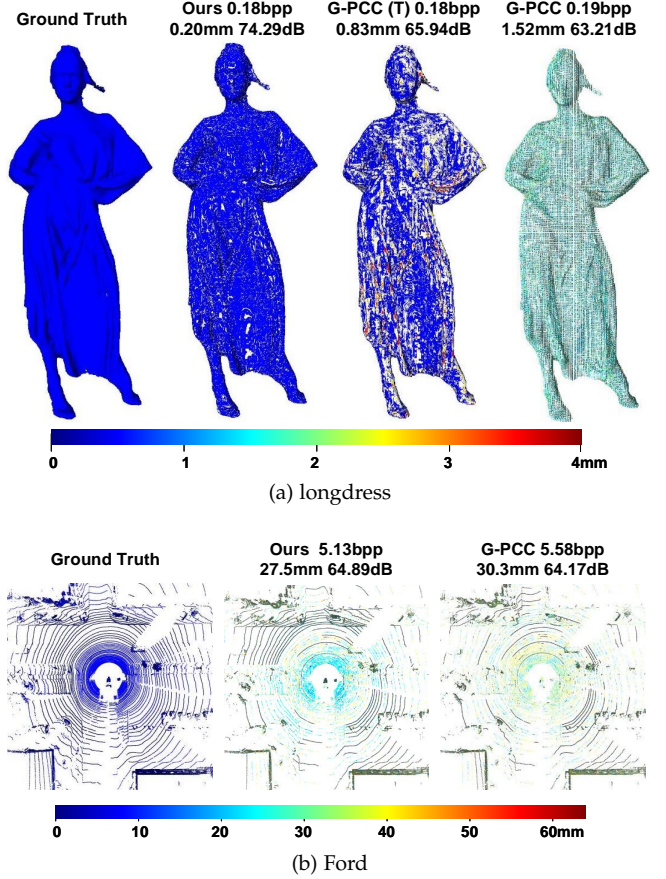


Fig. 13: Qualitative visualization of reconstruction of “longdress_vox10_1300” and “Ford_01_vox1mm_0500” for ground truth, Ours, and G-PCC. The color error map describes the point-to-point distortion measured in mm, and the numbers above represent the bitrate, mean error measured in mm, and D1 PSNR.

TABLE 4: Performance comparison of losslessly coded dense point clouds. Compression ratio is measured by the bpp gain.

Dense PCs	G-PCC	Ours	VoxelDNN [10], [26]		NNOC [25]	
			VoxelDNN	MsVoxelDNN	NNOC	fNNOC
red&black_vox10	1.08	0.72 (-33%)	0.66 (-39%)	0.87 (-20%)	0.73 (-32%)	0.88 (-18%)
loot_vox10	0.95	0.63 (-34%)	0.58 (-39%)	0.73 (-21%)	0.59 (-37%)	0.76 (-20%)
thaidancer_vox10	0.99	0.67 (-33%)	0.68 (-32%)	0.85 (-15%)	0.68 (-32%)	0.80 (-20%)
boxer_vox10	0.94	0.60 (-37%)	0.55 (-42%)	0.70 (-26%)	0.55 (-42%)	0.68 (-28%)
Average	0.99	0.65 (-34%)	0.62 (-38%)	0.79 (-20%)	0.64 (-36%)	0.78 (-21%)
Enc. Time (s)	4.0	9.5	885	54	191	106
Dec. Time (s)	1.0	9.1	640	58	1171	113

TABLE 5: BD-Rate gains measured using both D1 and D2 for the SparsePCGC against the G-PCC (T) using trisoup codec option, PCGCv2 [23], GeoCNNv2 [24], and ADL-PCC [9] for lossy coded dense point clouds.

Dense PCs	G-PCC (T)		PCGCv2 [23]		ADL-PCC [9]		GeoCNNv2 [24]	
	D1	D2	D1	D2	D1	D2	D1	D2
longdress_vox10_1300	-81.2%	-73.3%	-39.0%	-25.9%	-70.9%	-65.8%	-72.7%	-70.6%
red&black_vox10_1550	-86.4%	-76.3%	-42.3%	-24.1%	-70.1%	-63.0%	-66.8%	-65.3%
soldier_vox10_0690	-84.5%	-75.7%	-38.8%	-26.1%	-69.8%	-64.3%	-69.3%	-66.8%
loot_vox10_1200	-87.0%	-79.6%	-39.3%	-26.7%	-71.6%	-65.7%	-73.2%	-70.8%
queen_vox10_0200	-85.7%	-73.2%	-21.4%	-11.0%	-65.4%	-57.0%	-71.6%	-69.7%
player_vox11_0200	-92.7%	-84.2%	-39.9%	-31.1%	-76.5%	-72.1%	-78.8%	-76.6%
dancer_vox11_0001	-89.5%	-79.7%	-35.4%	-24.4%	-71.3%	-62.4%	-75.0%	-71.2%
Average	-86.7%	-77.4%	-36.6%	-24.2%	-70.8%	-64.3%	-72.5%	-70.1%

TABLE 6: BD-rate gains over the G-PCC anchor for lossy compressed sparse LiDAR PCG. Results are quoted from [14], [44] for comparison.

Sparse PCs	Ours	OctSqueeze [12]	VoxelCtxNet [14]
KITTI_vox2cm	-23.2%	-2.1%	-13.8%

ison. In the meantime, we directly reuse pretrained models of these methods because both VoxelDNN and NNOC (and their fast versions) include 8iVFB sequences (longdress, soldier) into the training, implying better compression performance on similar content in inference. On the contrary, we train our method on very different ShapeNet.

As seen, our method offers similar gains to the VoxelDNN and NNOC, e.g., 34% to 38%, when compared with the G-PCC anchor, but surpasses their fast versions with at least 10%. And, our method requires much less running time for encoding and decoding. For example, our approach speeds up the MsVoxelDNN at least 5x, and more than 10x to the fNNOC.

Lossy Compression of Dense PCGs. We then compare the SparsePCGC with the PCGCv2 [23], GeoCNNv2 [24], and ADL-PCC [9] for lossy compression of dense PCGs. Both GeoCNNv2 [24] and ADL-PCC [9] leverage the dense CNNs with the uniform voxel representation assumption. The PCGCv2 [23] is our earlier attempt to apply the multi-scale sparse tensor, in which it applies the fixed factors for resolution scaling, uses the lossless G-PCC to code low-scale samples, and just support the lossy compression of dense PCG. Both R-D curves in Fig. 12 and the BD-Rate gains in Table 5 evidence that the SparsePCGC present significant performance lead over these methods.

Lossy Compression of Sparse LiDAR PCGs. Most approaches adopt the octree model to represent sparse LiDAR point clouds. Huang *et al.* [12] proposed the OctSqueeze that uses the MLP to exploit the dependency between parent and

child nodes. Que *et al.* [14] then applied the uniform voxel model to represent the octree nodes in local neighborhood, and employed 3D CNN to exploit the dependency across them, which is dubbed as the VoxelCtxNet. As aforementioned, a coordinate refinement module that is close to our position offset adjustment was utilized in VoxelCtxNet to predict the coordinates of leaf nodes.

Since both OctSqueeze [14] and VoxelCtxNet [12] are not made publicly accessible, it is difficult for us to easily replicate their results. We directly quote the results of OctSqueeze. For the most recent VoxelContext-Net, luckily, another third party in MPEG standardization committee has re-implemented and re-run it following the MPEG CTC [44]. We use its results in Table 6, by which we best assure the same test conditions that are consented and suggested for standardization. For the same KITTI_vox2cm, our method shows 23.2% BD-Rate improvement, while the VoxelCtxNet (static) and OctSqueeze provide 13.8% and 2.1% gains respectively, again implying the advantages of our method.

7.4 Discussion

Due to various acquisition techniques used in different applications, the characteristics of input point clouds, including the density, volume, precision, noise, etc., vary greatly from one to another. It is extremely challenging to efficiently compress these diverse sources under the same model. As a compromise, existing solutions apply different models or tools to compress different inputs as aforementioned.

Previous sections reveal that the SparsePCGC, as a unified model, can generalize to compress diverse point clouds in either lossy or lossless mode efficiently. This is mainly because the proposed method can effectively exploit the sparsity nature of unstructured points:

- The SparseCNN deals with the points directly without assuming any prior knowledge of captured scene, which shall ideally support arbitrary-distributed points in a 3D space; Such point-wise

sparse convolution could significantly reduce the complexity; and the SparseCNN could best leverage valid neighbors within the receptive field to analyze and aggregate/embed local variations;

- And, multiscale representation leverages the resolution re-scaling to construct scale-wise hierarchy, with which we can effectively exploit cross-scale correlations to support long-range information embedding without imposing any additional desire of apriori knowledge of spatial structures.

We share models across all scales. Lossless SparsePCCG uses the 8-Stage SOPA model which only consumes 1.20 Mbytes. For lossy coded dense PCG, we use 1.20 Mbytes 8-Stage SOPA model in lossless phase, 2.72 Mbytes SLNE enhanced One-Stage SOPA, and 0.14Mbytes One-Stage SOPA in lossy phase; while for lossy coded sparse PCG, the lossless phase is the same, and 8.12 Mbytes SOPA (Position) model is used in lossy part.

8 CONCLUSION AND FUTURE WORK

The unified point cloud geometry compression approach is developed, showing the state-of-art performance in both lossless and lossy compression applications across a variety of datasets including the dense point clouds (8iVFB, Owlii) and the sparse LiDAR point clouds (KITTI, Ford) when compared with the MPEG G-PCC and other popular learning-based approaches. In the meantime, the proposed method shows lightweight computational complexity consumption because of the utilization of sparse convolution, and requires a small amount of storage for model parameters because we share the models across all scales.

The advantages of the proposed method come from the Sparse Tensor Processing based Multiscale Representation strategy, where we use sparse convolutions to directly deal with the unstructured points, and efficiently aggregate the local neighborhood information; and we also suggest the resolution scaling to enable multiscale representation to extensively exploit the cross-scale correlation.

There are a number of interesting topics for further exploration, including 1) the support of compression of color attributes; 2) 3D motion capturing for dynamic point clouds; and 3) better quality evaluation metric close to the human perceptual sensation for loss optimization.

REFERENCES

- [1] S. Schwarz, M. Preda, V. Baroncini et al., "Emerging mpeg standards for point cloud compression," *IEEE Journal on Emerging and Selected Topics in Circuits and Systems*, vol. 9, pp. 133–148, 2019. [1](#), [2](#), [5](#)
- [2] H. X. Nguyen, R. Trestian, D. To, and M. Tatipamula, "Digital twin for 5g and beyond," *IEEE Communications Magazine*, vol. 59, no. 2, pp. 10–15, 2021. [1](#)
- [3] D. Marpe, H. Schwarz, and T. Wiegand, "Context-based adaptive binary arithmetic coding in the h.264/avc video compression standard," *IEEE Transactions on Circuits and Systems for Video Technology*, vol. 13, no. 7, pp. 620–636, 2003. [1](#)
- [4] J. Pfaff, A. Filippov, S. Liu, X. Zhao, J. Chen, S. De-Luxán-Hernández, T. Wiegand, V. Rufitskiy, A. K. Ramasubramonian, and G. Van der Auwera, "Intra prediction and mode coding in vvc," *IEEE Transactions on Circuits and Systems for Video Technology*, pp. 1–1, 2021. [2](#)
- [5] D. Meagher, "Geometric modeling using octree encoding," *Computer graphics and image processing*, vol. 19, no. 2, pp. 129–147, 1982. [2](#)
- [6] C. Cao, M. Preda, V. Zakharchenko, E. S. Jang, and T. Zaharia, "Compression of sparse and dense dynamic point clouds—methods and standards," *Proceedings of the IEEE*, vol. 109, no. 9, pp. 1537–1558, 2021. [2](#)
- [7] M. Quach, G. Valenzise, and F. Dufaux, "Learning convolutional transforms for lossy point cloud geometry compression," in *IEEE ICIP*, 2019, pp. 4320–4324. [2](#), [5](#)
- [8] J. Wang, H. Zhu, H. Liu, and Z. Ma, "Lossy point cloud geometry compression via end-to-end learning," *IEEE Transactions on Circuits and Systems for Video Technology*, pp. 1–1, 2021. [2](#), [4](#), [5](#), [7](#), [9](#)
- [9] A. F. R. Guarda, N. M. M. Rodrigues, and F. Pereira, "Adaptive deep learning-based point cloud geometry coding," *IEEE Journal of Selected Topics in Signal Processing*, vol. 15, pp. 415–430, 2021. [2](#), [4](#), [5](#), [13](#), [14](#)
- [10] D. Nguyen, M. Quach, G. Valenzise, and P. Duhamel, "Multiscale deep context modeling for lossless point cloud geometry compression," *2021 IEEE International Conference on Multimedia Expo Workshops (ICMEW)*, 2021. [2](#), [4](#), [5](#), [13](#), [14](#)
- [11] T. Chen, H. Liu, Z. Ma, Q. Shen, X. Cao, and Y. Wang, "End-to-end learnt image compression via nonlocal attention optimization and improved content modeling," *IEEE Trans. Image Processing*, vol. 30, pp. 3179–3191, 2021. [2](#), [7](#), [8](#)
- [12] L. Huang, S. Wang, K. Wong, J. Liu, and R. Urtasun, "Octsqueeze: Octree-structured entropy model for lidar compression," *2020 IEEE/CVF Conference on Computer Vision and Pattern Recognition (CVPR)*, pp. 1310–1320, 2020. [2](#), [4](#), [5](#), [11](#), [14](#)
- [13] S. Biswas, J. Liu, K. Wong, S. Wang, and R. Urtasun, "Muscle: Multi sweep compression of lidar using deep entropy models," in *Advances in Neural Information Processing Systems*, vol. 33, 2020. [2](#), [5](#)
- [14] Z. Que, G. Lu, and D. Xu, "Voxelcontext-net: An octree based framework for point cloud compression," *2021 IEEE/CVF Conference on Computer Vision and Pattern Recognition (CVPR)*, 2021. [2](#), [4](#), [5](#), [10](#), [11](#), [14](#)
- [15] W. Yan, Y. Shao, S. Liu, T. H. Li, Z. Li, and G. Li, "Deep autoencoder-based lossy geometry compression for point clouds," *ArXiv*, vol. abs/1905.03691, 2019. [2](#)
- [16] T. Huang and Y. Liu, "3d point cloud geometry compression on deep learning," *Proceedings of the 27th ACM International Conference on Multimedia*, 2019. [2](#)
- [17] L. Gao, T. Fan, J. Wang, Y. Xu, and Z. Ma, "Point cloud geometry compression via neural graph sampling," *IEEE ICIP*, 2021. [2](#), [5](#)
- [18] C. Qi, L. Yi, H. Su, and L. Guibas, "Pointnet++: Deep hierarchical feature learning on point sets in a metric space," in *NIPS*, 2017. [2](#), [5](#)
- [19] S. Schwarz, P. A. Chou, and I. Sinharoy, "Jpeg pleno point cloud coding common test conditions," *ISO/IEC JTC1/SC29/WG11 N18474*, 2019. [2](#)
- [20] J. Pang, M. A. Lodhi, G. Martin-Cocher, and D. Tian, "Pcc: Ai-based point cloud compression for new PCC," *ISO/IEC JTC1/SC29/WG11 (MPEG/JPEG) m56776*, April 2021. [2](#)
- [21] C. Choy, J. Gwak, and S. Savarese, "4d spatio-temporal convnets: Minkowski convolutional neural networks," in *IEEE CVPR*, 2019. [3](#), [5](#)
- [22] G. Bjørtegaard, "Calculation of average PSNR differences between rd-curves," in *ITU-T SG 16/Q6, 13th VCEG Meeting*. document VCEG-M33, April 2001. [4](#)
- [23] J. Wang, D. Ding, Z. Li, and Z. Ma, "Multiscale point cloud geometry compression," *2021 Data Compression Conference (DCC)*, pp. 73–82, 2021. [4](#), [6](#), [7](#), [9](#), [10](#), [13](#), [14](#)
- [24] M. Quach, G. Valenzise, and F. Dufaux, "Improved deep point cloud geometry compression," *2020 IEEE MMSP Workshop*, 2020. [4](#), [13](#), [14](#)
- [25] E. C. Kaya and I. Tabus, "Neural network modeling of probabilities for coding the octree representation of point clouds," *IEEE MMSP*, 2021. [4](#), [13](#), [14](#)
- [26] D. Nguyen, M. Quach, G. Valenzise, and P. Duhamel, "Lossless coding of point cloud geometry using a deep generative model," *IEEE Transactions on Circuits and Systems for Video Technology*, 2021. [4](#), [5](#), [13](#), [14](#)
- [27] WG7, MPEG 3D Graphics Coding, "Performance analysis of currently ai-based available solutions for pcc," *ISO/IEC JTC 1/SC 29/WG 7 N0174*, July 2021. [4](#)

- [28] C. L. Jackins and S. L. Tanimoto, "Oct-trees and their use in representing three-dimensional objects," *Computer Graphics and Image Processing*, vol. 14, no. 3, pp. 249–270, 1980. [4](#)
- [29] R. Schnabel and R. Klein, "Octree-based point-cloud compression," in *Eurographics*, 2006. [4](#)
- [30] Y. Huang, J. Peng, C. C. Kuo, and M. Gopi, "A generic scheme for progressive point cloud coding," *IEEE Transactions on Visualization and Computer Graphics*, vol. 14, no. 2, pp. 440–453, 2008. [4](#)
- [31] K. Mammou, P. A. Chou, D. Flynn, M. Krivokuća, O. Nakagami, and T. Sugio, "G-PCC codec description v2," *ISO/IEC JTC1/SC29/WG11 N18189*, 2019. [4](#)
- [32] D. Graziosi, O. Nakagami, S. Kuma, A. Zaghetto, T. Suzuki, and A. Tabatabai, "An overview of ongoing point cloud compression standardization activities: video-based (v-pcc) and geometry-based (g-pcc)," *APSIPA Transactions on Signal and Information Processing*, vol. 9, 2020. [4](#)
- [33] W. Zhu, Z. Ma, Y. Xu, L. Li, and Z. Li, "View-dependent dynamic point cloud compression," *IEEE Transactions on Circuits and Systems for Video Technology*, vol. 31, no. 2, pp. 765–781, 2020. [5](#)
- [34] C. Szegedy, S. Ioffe, V. Vanhoucke, and A. A. Alemi, "Inception-v4, inception-resnet and the impact of residual connections on learning," in *AAAI*, 2017. [7](#)
- [35] J. Ballé, D. Minnen, S. Singh et al., "Variational image compression with a scale hyperprior," in *ICLR*, 2018. [8, 9](#)
- [36] D. Minnen, J. Ballé, and G. D. Toderici, "Joint autoregressive and hierarchical priors for learned image compression," in *IEEE NeurIPS*, 2018, pp. 10 771–10 780. [7](#)
- [37] A. X. Chang, T. Funkhouser, L. Guibas, P. Hanrahan et al., "Shapenet: An information-rich 3d model repository," *ArXiv*, vol. abs/1512.03012, 2015. [10](#)
- [38] J. Behley, M. Garbade, A. Milioto, J. Quenzel, S. Behnke, C. Stachniss, and J. Gall, "Semantickitti: A dataset for semantic scene understanding of lidar sequences," 2019 IEEE/CVF International Conference on Computer Vision (ICCV), pp. 9296–9306, 2019. [10](#)
- [39] "Mpeg pcc dataset," <http://mpegfs.int-evry.fr/mpegcontent/>, accessed: 2021. [11](#)
- [40] WG7, "Common test conditions for g-pcc," *ISO/IEC JTC1/SC29/WG11 N00106*, 2021. [11](#)
- [41] 3DG, "G-pcc tmc13v12 performance evaluation and anchor results," *ISO/IEC JTC1/SC29/WG7 MDS19615*, 2021. [11](#)
- [42] "Mpeg-pcc-tmc13," <https://github.com/MPEGGroup/mpeg-pcc-tmc13>, accessed: 2021. [11](#)
- [43] "Minkowskiengine," <https://github.com/NVIDIA/MinkowskiEngine>, accessed: 2021. [11](#)
- [44] M. A. Lodhi, J. Pang, and D. Tian, "[ai-3dgc] point cloud geometry compression using learned octree entropy coding," *ISO/IEC JTC 1/SC 29/WG 7 M58167*, Oct 2021. [14](#)

9 SUPPLEMENTARY INFORMATION

9.1 The Diversity of Various Point Clouds

Due to various acquisition techniques used in different applications, the characteristics of input point cloud source, including its density, volume, precision, noise, etc., vary greatly from one to another. The point clouds sampled from depth images or meshes are usually with very dense points, e.g., 8iVFB sequences in Fig. 14a, which are presented with smooth surface and often used for immersive media in AR/VR applications. The point clouds collected by LiDAR are typically very sparse with higher geometry precision, e.g., KITTI sequences in Fig. 14b, which are usually set for localization and map navigation in autonomous machine.

As shown in Fig. 15a, the dense 8iVFB samples have around 1 million points with 10-bit precision; and the number of points increases with the increase of the precision, which suggests that we can upscale the POVs from preceding scale to approximate current-scale MP-POVs.

On the contrary, the sparse KITTI_vox1mm sample has 18-bit precision but only 120k points; And the number of points is almost the same on high-precision scales (e.g., from 14 bit to 18 bit), suggesting that we just need to estimate the position of occupied voxels.

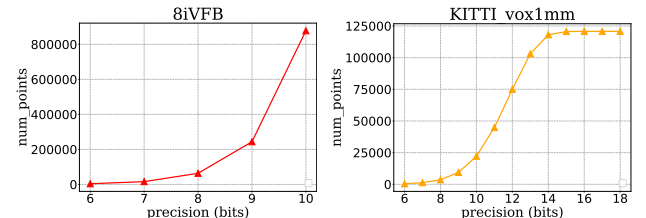
Note that the number of points at the highest precision scale is from the input PCG, and the number of points at lower precision scales is counted from dyadically-downscaled PCG.

We further show the density in Fig. 15b by normalizing the number of points at each precision scale to the resolution. It is obvious that 8iVFB has a high density (≈ 1) while KITTI_vox1mm exhibits much lower density (≈ 0). Having lower point density makes it hard to explore neighborhood correlation for compression. This explains why the compression gains of sparse point clouds is lower than that of dense point clouds. And the point cloud becomes denser when it

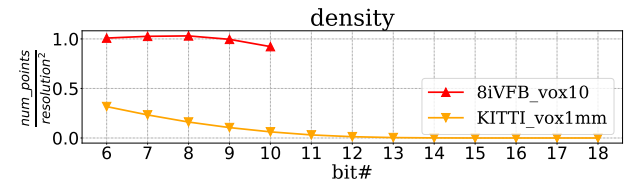
is downscaled, especially for the KITTI_vox1mm, implying a better compressed low-scale point clouds can be useful for cross-scale prediction.



Fig. 14: **Point Cloud Examples.** (a) dense point clouds 8iVFB; (b) Sparse LiDAR point clouds KITTI.



(a) Number of points at each precision scale.



(b) Density at each precision scale.

Fig. 15: Comparison of the number of points and density of different point clouds.